

**A new zeolitic hydroxymethylimidazolate material and its use in mixed matrix membranes based on 6FDA-DAM for gas separation**

Adelaida Perea-Cachero,<sup>a</sup> Javier Sánchez-Laínez,<sup>a</sup> Ángel Berenguer-Murcia,<sup>b</sup> Diego Cazorla-Amorós,<sup>b</sup> Carlos Téllez<sup>a</sup> and Joaquín Coronas<sup>a,\*</sup>

<sup>a</sup> Chemical and Environmental Engineering Department and Instituto de Nanociencia de Aragón (INA), Universidad de Zaragoza, 50018 Zaragoza, Spain

<sup>b</sup> Alicante Materials Institute and Inorganic Chemistry Department, University of Alicante, 03080 Alicante, Spain

\*Corresponding author.

E-mail address: coronas@unizar.es

**Abstract:** The new ZIF named UZAR-S13 is formed by  $Zn^{2+}$  and 4(5)-(hydroxymethyl)imidazolate. UZAR-S13 has two distinct phases according to SEM and XRD: amorphous spheres and sheet crystals. UZAR-S13 and byproducts, with no  $N_2$  adsorption, rendered a notable  $CO_2$  uptake (up to  $3.8 \text{ mmol g}^{-1}$  at 30 bar and  $0 \text{ }^\circ\text{C}$ ), approaching values of known ZIFs. The most promising materials were included as fillers in mixed matrix membranes based on copolyimide 6FDA-DAM to study the separation of  $CO_2/CH_4$ ,  $CO_2/N_2$ ,  $H_2/CO_2$  and  $H_2/CH_4$ . The pore blocking hindered the gas flow of bulky molecules ( $CH_4$ ,  $N_2$  and  $CO_2$ ). The high  $CO_2$  adsorption on sheet crystals also contributed to the decrease in the permeability of  $CH_4$ ,  $N_2$  and  $CO_2$ , giving poor selectivities. In contrast, the MMMs improved both the  $H_2/CH_4$  selectivity (8.9-12.7 vs. 7.2) and permeability of  $H_2$  (544-597 vs. 505 Barrer) of the bare 6FDA-DAM membrane. This emphasizes the potential application of the fillers in the separation by molecular sieving of gas mixtures without  $CO_2$ .

**Keywords:** MOF, ZIF, copolyimide 6FDA-DAM, mixed matrix membrane, gas separation

## 1 Introduction

CO<sub>2</sub> is the main greenhouse gas and its accumulation in the atmosphere is causing the so-called global warming phenomenon. The necessity of CO<sub>2</sub> separation has arisen as a consequence of the damage caused by emissions from power generation, industrial processes, de-carbonization and transportation [1]. Carbon capture and storage (CCS) is the principal approach to reduce CO<sub>2</sub> levels in the environment [2, 3]. The crucial stage in this process is the separation of CO<sub>2</sub> from other gases before it reaches the atmosphere [2]. In addition, CO<sub>2</sub> is an impurity present in fuel gases, such as natural gas or biogas, which diminishes the heating value of fuels and causes corrosion in pipelines [4, 5]. In this context, natural gas and H<sub>2</sub> are being explored as alternative energy resources and carriers since they have high heating values [6]. Natural gas, mainly composed of CH<sub>4</sub>, is a desirable fuel for transportation [7]. Its combustion produces the least CO<sub>2</sub> emissions per energy since CH<sub>4</sub> is the hydrocarbon with the highest H/C ratio [7]. Natural gas is considered as a transition fuel while H<sub>2</sub> technology is progressing [6]. Promising techniques have been developed to achieve effective CO<sub>2</sub> separation in CCS and natural gas purification as well as CH<sub>4</sub> separation in H<sub>2</sub> purification. Gas separation membranes are considered as a less energy-demanding and more efficient technology than conventional methods [2, 8, 9]. Commercial gas separation through membrane technology is dominated by polymeric membranes due to their low cost, easy processability and mechanical stability [3, 10]. However, polymeric membranes present a trade-off between permeability and selectivity [10]. In mixed matrix membranes (MMMs), porous particles (fillers) are included in polymers to combine the advantages of both phases, these being high selectivities and permeation fluxes [8, 10]. While zeolites, mesoporous silica and carbon molecular sieves have been widely employed as fillers, metal-organic frameworks (MOFs) and zeolitic imidazolate frameworks (ZIFs) have recently been incorporated into MMMs [11-13].

MOFs, also known as porous coordination polymers (PCPs), are hybrid porous networks formed by the coordination of metal ions or clusters and organic ligands resulting in one-, two- or three-dimensional (1D, 2D or 3D) structures [14]. MOFs feature exceptional surface areas, high pore volumes, considerable thermal and chemical stability, permanent porosity and flexibility [10]. Besides, the broad diversity of metals and organic ligands has given rise to a number of MOFs with different structures and characteristics [15-17]. The size, shape and chemical surface of the pores, and thus the properties of the MOF, can be tailored by selecting the appropriate metallic and organic species [15-17]. ZIFs constitute an interesting subfamily of MOFs. Their framework is composed of divalent metal ions ( $Zn^{2+}$ ,  $Co^{2+}$ ,  $Cu^{2+}$ , etc.) and imidazolate-type ligands. The coordination of the metallic and organic components gives tetrahedral subunits whose arrangement leads to a zeolitic topology, i.e. the M-Im-M angle (M, metal; Im, imidazolate) in ZIFs and the Si-O-Si angle typically found in zeolites are similar ( $145^\circ$ ) [18]. Consequently, ZIFs combine properties of both MOFs and zeolites, such as superior thermal and chemical stabilities [19, 20], microporosity [20], large surface areas [19, 20], diversity of frameworks [21], wide range of pore sizes [22], and post-functionalization [21]. All these properties make ZIFs attractive candidates for gas separation, especially by adsorption and membrane technologies [22]. In this respect, ZIFs have shown remarkable  $CO_2$  capacities [23] and promising separation performances for several binary gas mixtures containing  $CO_2$  which are relevant in different industrial processes [19, 23].

In recent years, the interest in crystalline layered materials has been increasing because their 2D character provides them with extraordinary physicochemical properties [24] such as size- and shape-dependent electronic and optical properties [25], mechanical strength [25], high surface areas [25], and excellent heat conduction [26]. As a consequence, 2D materials are employed in a vast range of applications in fields such as sensing [27], catalysis [27], molecular recognition [28], energy storage [27, 29], (opto)electronics [30] and gas separation [31, 32]. This in turn has provoked the current interest in the preparation of 2D nanostructured MOFs.

Layered MOFs could be of great importance for selective gas adsorption [29, 33, 34] since lamellar compounds are able to accommodate guest molecules between the layers [35] while their hybrid nature allows tunable guest-framework interactions [33]. As an example of enhancement with layered MOFs, Rodenas *et al.* prepared MMMs with CuBDC (2D structure) nanosheets as a filler achieving a selectivity between 7.5 and 8 times higher than those of bulk CuBDC MMMs [29]. Moreover, upon delamination, layered MOFs can give rise to ultrathin selective membranes [36].

The synthesis and characterization of UZAR-S13 (henceforth referred to as S13\_sph&sh), a new ZIF, is reported here. S13\_sph&sh is formed after the reaction at mild temperature of Zn<sup>2+</sup> and 4(5)-(hydroxymethyl)imidazolate (hmlm, see Figure 1) in a 1:3.3 molar ratio giving rise to two distinct phases related to the shape (spheres and sheets). The hmlm ligand was selected because its hydroxyl functional group was thought to influence the capability of interaction with small gas molecules such as CO<sub>2</sub> [37]. Spheres and sheets are obtained separately by modifying the metal:ligand ratio. Sheet-shaped crystals are also achieved when the reaction is carried out at room temperature maintaining the original metal:linker ratio (S13\_sheet\_RT). CO<sub>2</sub> adsorption studies at low and high pressure were carried out on these samples. The sheet shape of crystals of S13\_sph&sh and S13\_sheet\_RT and their CO<sub>2</sub> affinity opened up the possibility of their application in membranes for CO<sub>2</sub> separation. Thus, MMMs were prepared using S13\_sph&sh and S13\_sheet\_RT as fillers and copolyimide 6FDA-DAM as the polymeric matrix. 6FDA (2,2-bis(3,4-carboxyphenyl) hexafluoropropane dianhydride)-based polyimides have shown excellent properties ranging from mechanical strength, chemical and thermal stability, and spinnability to high gas permeability and selectivity [38]. Such good gas permeation properties are produced by the presence of fluorinated side groups (-C(CF<sub>3</sub>)<sub>2</sub>-) (see Figure 1b). These bulky and hydrophobic groups can affect the gas solubility in the membranes, the chain rigidity, the internal rotation of bonds, molecular distances, and the free volume between the polymer chains [39]. The MMMs obtained were employed in the

separation of CO<sub>2</sub>/CH<sub>4</sub>, CO<sub>2</sub>/N<sub>2</sub>, H<sub>2</sub>/CO<sub>2</sub> and H<sub>2</sub>/CH<sub>4</sub> mixtures, typical of natural gas, post-combustion, pre-combustion and H<sub>2</sub> purification processes.

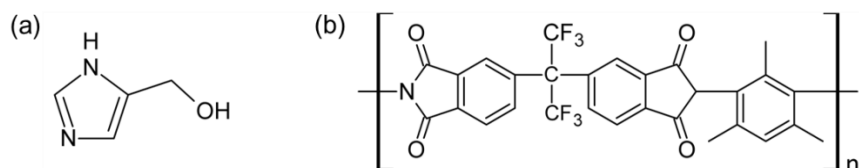


Figure 1. Chemical structure of (a) 4(5)-(hydroxymethyl)imidazole (hmlm-H) and (b) 6FDA-DAM.

## 2 Experimental section

### 2.1 Methods and materials

Anhydrous chloroform (CHCl<sub>3</sub>, ≥99 %, Sigma-Aldrich), *N,N*-dimethylformamide (DMF, HCON(CH<sub>3</sub>)<sub>2</sub>, 99.5 %, Scharlau), 4(5)-(hydroxymethyl)imidazole (hmlm-H, C<sub>4</sub>H<sub>6</sub>N<sub>2</sub>O, 97 %, Aldrich) and zinc acetate dihydrate (Zn(CH<sub>3</sub>COO)<sub>2</sub>·2H<sub>2</sub>O, 98 %, Sigma-Aldrich) were used as received without further purification. 6FDA-DAM (418 000 Da) polymer was purchased from Akron Polymer Systems, Inc. and prepared using the monomers 6FDA and DAM (diaminomesitylene).

### 2.2 Synthesis of S13\_sph&sh

In a typical synthesis, 0.1580 g of zinc acetate dihydrate and 0.2354 g of hmlm-H were dissolved in 8 mL and 10 mL of DMF, respectively (the molar metal:linker ratio was 1:3.3). The metal solution was poured on the ligand solution and the mixture was stirred for 5 min. Subsequently, the resulting solution was placed in a stainless steel Teflon™-lined autoclave. The autoclave was transferred into a conventional oven preheated at 100 °C where it was kept for 12 h. After cooling to ambient temperature, the product was collected by centrifugation at 10 000 rpm and washed 3 times with fresh DMF. Finally, it was dried for 2 d at room temperature.

### 2.3 Synthesis of S13\_sphere\_1:1, S13\_sphere\_1:2, S13\_sheet and S13\_sheet\_RT

In order to obtain separately the spheres and sheets observed in S13\_sph&sh, the metal:ligand ratio was modified to 1:10, 1:2 and 1:1 achieving S13\_sheet, S13\_sphere\_1:2 and S13\_sphere\_1:1, respectively. All these products were prepared and rinsed according to the procedure used for S13\_sph&sh. For the same purpose, the synthesis conditions were modified decreasing the temperature and augmenting the reaction time, but keeping the metal:linker ratio from S13\_sph&sh, giving S13\_sheet\_RT. In this case, the hmlm solution was prepared in a glass vial. Then the metal solution was added. The mixture was stirred for 5 min. The reaction was carried out under static conditions at room temperature. After 21 d, the product was recovered by centrifugation at 10 000 rpm, washed 3 times with DMF and dried at ambient conditions. Yields of these products as well as that of S13\_sph&sh are presented in Table S1. The yields were calculated as an average of at least two syntheses. It is worth mentioning that a reaction time of 14 d in the synthesis of 1\_sheet\_RT gave the same kind of sheets but slightly smaller. Thus we chose 21 d in order not to prolong excessively the reaction time, believing that the size of the sheets would hardly have changed with longer times.

### 2.4 Activation of S13\_sph&sh, S13\_sphere\_1:1 and S13\_sheet\_RT

Samples S13\_sph&sh, S13\_sphere\_1:1 and S13\_sheet\_RT were activated by means of a solvent-exchange process. First, the products were immersed in anhydrous chloroform at room temperature under stirring. The chloroform was refreshed every 24 h. After 7 d, the solvent was removed by centrifugation. The solids were rinsed 3 times with fresh chloroform and dried at ambient conditions. They were then treated under vacuum at 80 °C (140 °C in the case of S13\_sphere\_1:1) for 8 h with heating and cooling rates of 1 °C min<sup>-1</sup>, producing S13\_sph&sh\_act, S13\_sphere\_1:1\_act and S13\_sheet\_RT\_act. The elemental analysis calculated for S13\_sph&sh\_act ( $\text{Zn}(\text{C}_4\text{H}_5\text{N}_2\text{O})_2 \cdot \text{H}_2\text{O} = \text{C}_8\text{H}_{12}\text{N}_4\text{O}_3\text{Zn}$ ), i.e. C, 34.62; H, 4.36; N,

20.18, was in good agreement with the values experimentally found by elemental analysis, i.e. C, 36.74; H, 4.67; N, 19.97.

## 2.5 MMM preparation

Prior to MMM preparation, 6FDA-DAM in thread form was dried at 100 °C overnight. Samples S13\_sph&sh and S13\_sheet\_RT were employed as recovered after chloroform exchange (before vacuum treatment). The solids were dispersed in anhydrous chloroform in such a way that the ZIF loading in the polymeric matrix was 10 wt%. The calculated amount of 6FDA-DAM was then added. The mixture was stirred overnight. The casting solution was subjected to three cycles of sonication and stirring (the sonication and stirring lasted 15 minutes each in each cycle). The suspension was cast into a Petri dish at room temperature. The Petri dish was capped so that the solvent slowly evaporated. Occluded chloroform molecules were readily removed upon heating at 100 °C for 1 d. The membranes prepared with the pure polymer, S13\_sph&sh and S13\_sheet\_RT had a thickness of  $64 \pm 13 \mu\text{m}$ ,  $68 \pm 8 \mu\text{m}$  and  $74 \pm 3 \mu\text{m}$ , as measured with a Digimatic Micrometer. These values were determined by averaging the results of the same kind of membranes after 3-4 measurements per membrane.

## 2.6 Binary gas separation experiments

Permeability tests were carried out to study the separation performance of the MMMs prepared in this work. The membranes,  $3.14 \text{ cm}^2$  in area, were supported on a 316LSS macroporous disk inside a stainless steel module and gripped with Viton® O-rings. The macroporous support had a nominal pore size of  $20 \mu\text{m}$  and was purchased from Mott Corporation. Experiments were carried out at 35 °C inside an oven to control the temperature. Equimolar  $\text{CO}_2/\text{CH}_4$ ,  $\text{H}_2/\text{CO}_2$  and  $\text{H}_2/\text{CH}_4$  and 10/90 vol%  $\text{CO}_2/\text{N}_2$  gas mixtures were fed into the module at 3.0 bar through two mass-flow controllers (Alicat Scientific, MC-100CCM-D) with a total volumetric flow of 50 and  $100 \text{ cm}^3(\text{STP}) \text{ min}^{-1}$ , respectively. The permeate side was swept at 1.2 bar with a  $2 \text{ cm}^3(\text{STP}) \text{ min}^{-1}$  stream of He ( $4.5 \text{ cm}^3(\text{STP}) \text{ min}^{-1}$  for the pure 6FDA-DAM

membrane) regulated by a mass-flow controller (Alicat Scientific, MC-5CCM-D). The permeate stream was analyzed by means of an Agilent 3000A online gas microchromatograph equipped with a thermal conductivity detector (TCD) to determine the concentration of both gas components. Measurements were taken once the steady state was achieved (at around 1.5 h). Permeability values were expressed in Barrer units ( $1 \text{ Barrer} = 10^{-10} \text{ cm}^3(\text{STP}) \text{ cm} (\text{cm}^{-2} \text{ s}^{-1} \text{ cmHg}^{-1}) = 7.5 \times 10^{-18} \text{ m}^3(\text{STP}) \text{ m} (\text{m}^{-2} \text{ s}^{-1} \text{ Pa}^{-1})$ ). Membrane selectivity,  $S_{i/j}$ , was calculated as the ratio of the permeability of the component  $i$  over that of the component  $j$ .

## 2.7 Characterization

Fourier transform infrared (FTIR, Shimadzu IRAffinity-1) spectra of bulk samples were recorded using the KBr disk technique in a wavenumber range of 4000-400  $\text{cm}^{-1}$ . Attenuated total reflectance Fourier transform infrared (ATR-FTIR, Bruker Vertex 70 FTIR) spectra of the MMMs were recorded between 4000 and 600  $\text{cm}^{-1}$ . The resolution of both FTIR and ATR-FTIR spectra was 4  $\text{cm}^{-1}$ . Thermogravimetric analyses (TGA, Mettler Toledo TGA/DSC 1 SF/755) were performed with a heating ramp of 5  $^{\circ}\text{C min}^{-1}$  from 25 to 900  $^{\circ}\text{C}$  in air atmosphere. The glass transition temperature ( $T_g$ ) of the MMMs was determined by differential scanning calorimetry (DSC, Mettler Toledo DSC822<sup>e</sup>). The MMMs were scanned in two consecutive runs from 25 to 450  $^{\circ}\text{C}$  using a heating rate of 20  $^{\circ}\text{C min}^{-1}$  in air. The value of  $T_g$  was calculated from the heat flow curve as the temperature in the inflexion point of the second run in order to remove the thermal and mechanical history of the samples. Bulk products as well as the MMMs were characterized by powder X-ray diffractometry (PXRD, D-Max Rigaku and Bruker D8 Advance). PXRD patterns were gathered at ambient temperature with a copper anode using a graphite monochromator to select  $\text{CuK}\alpha$  radiation with  $\lambda = 1.5418 \text{ \AA}$ . Scanning electron microscopy (SEM, FEI Inspect F50) studies of the samples were carried out in a voltage range of 2-5 kV. The samples were coated with platinum under vacuum conditions. For cross-section SEM images of the MMMs, small pieces of membranes were broken inside a liquid  $\text{N}_2$  bath (freeze-fracturing)



to produce a clean cross sectional surface. Crystal thicknesses were measured by means of the ImageJ [40] software using SEM images. Brunauer-Emmett-Teller (BET) specific surface areas were determined from N<sub>2</sub> sorption isotherms at -196 °C (Tristar 3000). CO<sub>2</sub> adsorption isotherms at low pressure (Micromeritics ASAP 2020 V1.04H) were collected at 25 °C. Samples (*ca.* 150 mg) for CO<sub>2</sub> (low pressure) and N<sub>2</sub> sorption were previously degassed at 80 °C for 8 h with a heating rate of 1 °C min<sup>-1</sup>. High pressure carbon dioxide and hydrogen adsorption measurements were done in an automatic volumetric apparatus (Quantachrome iSorb HP1) to perform carbon dioxide isotherm experiments up to 45 bar and hydrogen isotherm experiments up to 200 bar. The manifold of the apparatus was kept at 36 °C. For the CO<sub>2</sub> experiments, a circulator bath set to 0 or 40 °C was employed to ensure a constant adsorption cell temperature. In the case of hydrogen, the sample cell was kept at 25 °C by means of a liquid bath. The manifold volume was calibrated with a standard volume, using helium as a calibrating fluid. To ensure that the apparatus was leak-free, hydrogen leak tests were executed at 90 and 150 bar for 28 h, the resulting leak rate being below 10<sup>-6</sup> Torr (Torr<sup>-1</sup> s<sup>-1</sup>). The bulk gas amounts were obtained using the modified Benedict-Webb-Rubin equation of state [41] and the cell volume was obtained considering the correction described in the literature [42]. Prior to all the adsorption experiments, the samples were degassed at 150 °C for 4 h under vacuum. After that, the sample was loaded in the sample holder, and then evacuated at 150 °C for another 4 h under vacuum. Sample masses ranged between 0.5 and 1.0 g to ensure accurate measurements. Excess adsorption was obtained in both CO<sub>2</sub> and H<sub>2</sub> sorption measurements at high pressure. Elemental analysis (Thermo Flash 1112) was carried out to reveal the C, H and N composition of the samples.

### 3 Results and discussion

#### 3.1 Characterization of S13\_sph&sh, S13\_sphere\_1:1, S13\_sphere\_1:2, S13\_sheet and S13\_sheet\_RT

The chemical formula of ZIFs is commonly  $M(\text{Im})_2$  (where Im denotes any type of imidazolate ligand) [43, 44]. The formula of S13\_sph&sh, established taking into account the results obtained in TGA characterization, is  $\text{Zn}(\text{hmlm})_2 \cdot x\text{DMF} \cdot y\text{H}_2\text{O}$ , where typically  $x = 0.15$  and  $y = 1.0$ . In the case of S13\_sph&sh\_act, elemental analysis and TGA data were used to corroborate its chemical formula:  $\text{Zn}(\text{hmlm})_2 \cdot z\text{H}_2\text{O}$  (normally,  $z = 0.5$ ). Calculations were carried out using TGA curves of 4 and 5 samples for S13\_sph&sh and S13\_sph&sh\_act, respectively. The different values acquired from the thermograms were utilized as an average in order to achieve an accurate solution. Figure 2 shows the TGA and differential thermogravimetric (DTG) curves of S13\_sph&sh and S13\_sph&sh\_act. The first weight loss at 25-100 °C in both samples is due to water release and has a value of 6.2 and 3.6 % (calcd. 6.2 and 3.2 %), respectively. In S13\_sph&sh, a second step of 3.4 % between 100 and 175 °C is found and is attributed to DMF loss (calcd. 3.8 %). S13\_sph&sh\_act does not possess such a step. The decomposition of both samples takes place from *ca.* 175 °C. FTIR characterization corroborates the presence of a small amount of DMF molecules in S13\_sph&sh (Figure S1). The band placed at  $1660 \text{ cm}^{-1}$  is ascribed to the C=O stretching from DMF [45]. This band disappeared for S13\_sph&sh\_act. This confirms that S13\_sph&sh\_act was successfully activated, as expected from the TGA results.

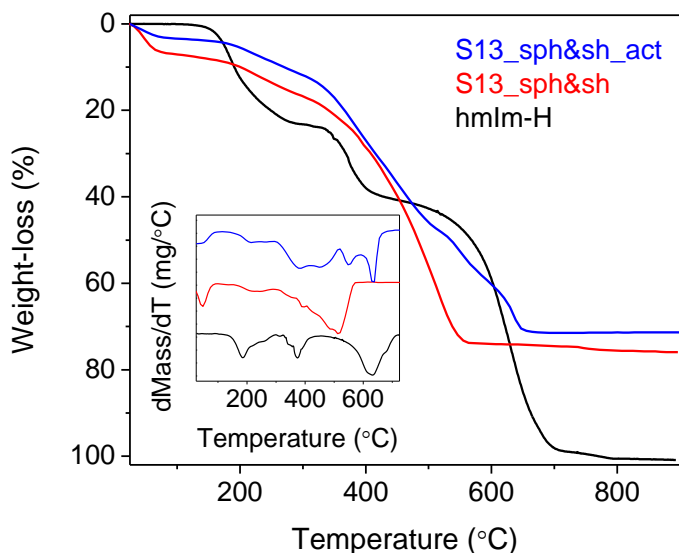


Figure 2. TGA and DTG curves of hmlm-H, S13\_sph&sh and S13\_sph&sh\_act.

As shown in the SEM images (and confirmed by PXRD patterns), two phases are well-differentiated in S13\_sph&sh (Figure 3a). The first is composed of spherical particles with a size ranging between 0.7 and 2.5  $\mu\text{m}$ . The second and majority phase contains large layers composed of sheet blocks with edges of around 1  $\mu\text{m}$  (see inset).

In order to obtain both phases separately, different syntheses were carried out varying the molar metal:ligand ratio. The ratio for S13\_sph&sh had a value of 1:3.3. When this was increased up to 1:2 and 1:1 (S13\_sphere\_1:2 and S13\_sphere\_1:1), only spheres were obtained (Figure 3b and 3c). The size distribution is heterogeneous with particles larger than spheres of S13\_sph&sh (approximately 1.0-5.5  $\mu\text{m}$  in diameter). It is worth mentioning that S13\_sphere\_1:1 is a purer phase than S13\_sphere\_1:2, as observed by microscopy (and verified by PXRD), because the latter has a larger number of irregular particles along with the spheres. On the other hand, diminishing the metal:linker ratio down to 1:10 led to rectangular sheets with round vertices and submicrometric edges (Figure 3d). Flat particles were also obtained when the synthesis conditions were adjusted keeping the molar ratio of S13\_sph&sh

(S13\_sheet\_RT). The reaction at room temperature for 21 d gives rise to larger sheets (1.0-3.5  $\mu\text{m}$ ). After drying at ambient conditions, crystals exposed to the atmosphere were arranged forming rosettes (Figure 3e) while crystals in contact with the glass dish were arranged with the larger face parallel to the surface (Figure 3f).

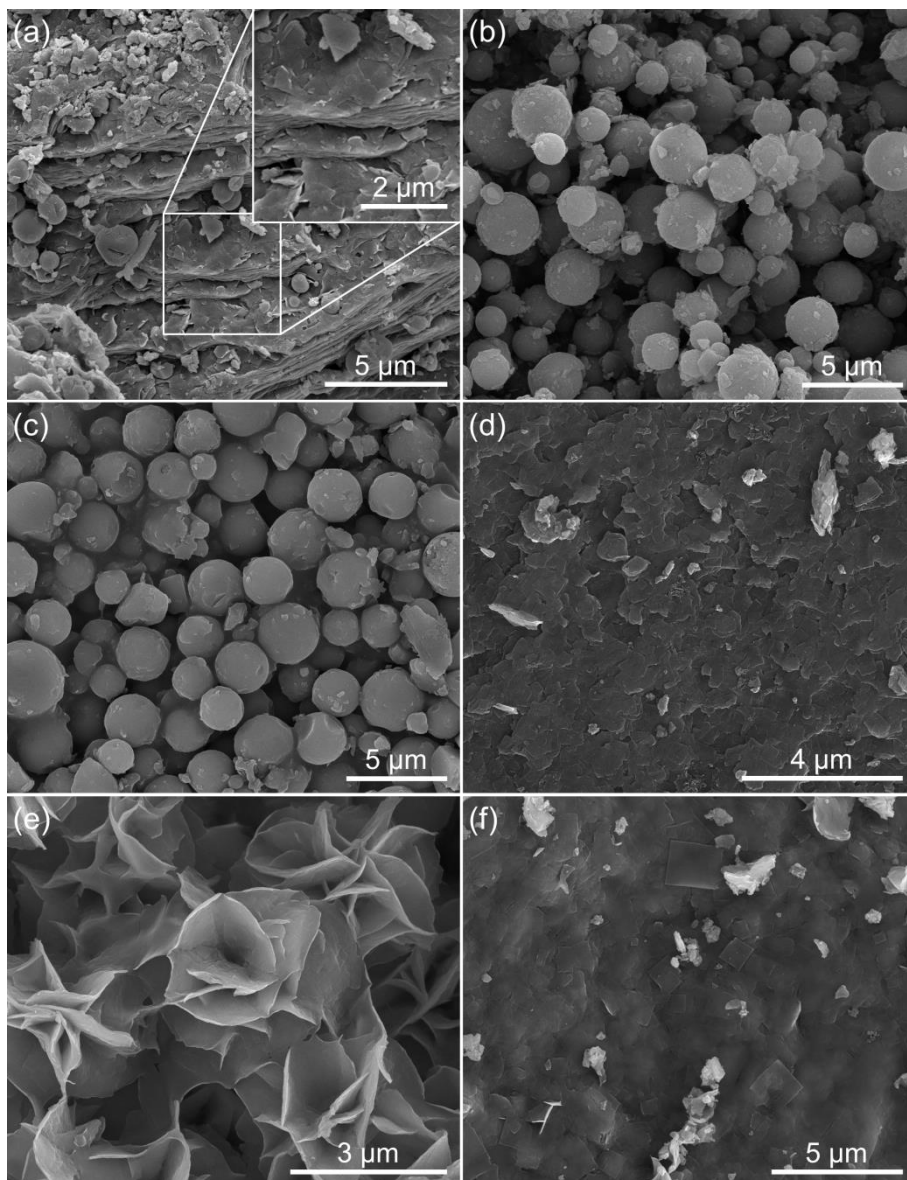


Figure 3. SEM images of (a) S13\_sph&sh, (b) S13\_sphere\_1:2, (c) S13\_sphere\_1:1, (d) S13\_sheet, (e) crystals of S13\_sheet\_RT exposed to the atmosphere (rosettes) and (f) in contact with dish surface.

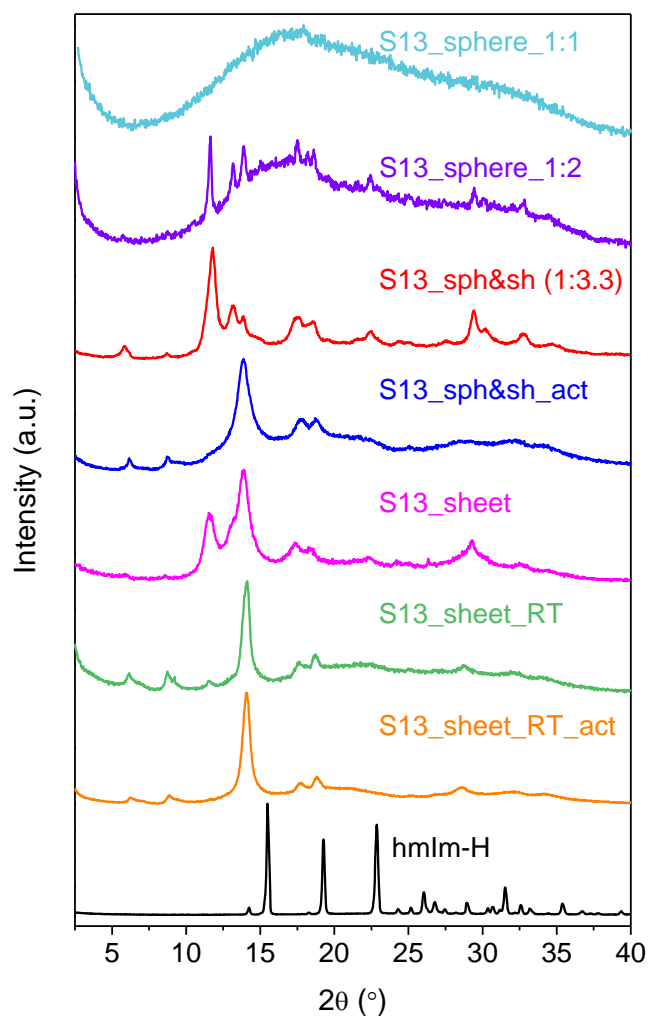


Figure 4. PXRD patterns of some products synthesized in this study and that of hmlm-H. The molar metal:ligand ratio of S13\_sph&sh is shown between parentheses.

PXRD patterns of the samples prepared in this work are depicted in Figure 4. It was not possible to solve their crystal structures by single crystal X-ray diffraction as single crystals were not obtained. PXRD data was not useful either, because of the scarcity of diffraction peaks and their broad width. As mentioned above, PXRD studies corroborate that S13\_sph&sh possesses two distinct phases: spheres and sheets. The spheres (S13\_sphere\_1:2 and S13\_sphere\_1:1) constitute an amorphous phase whereas the sheets (S13\_sheet) define the crystalline phase. S13\_sheet and S13\_sph&sh\_act maintain the peak positions from

S13\_sph&sh (see Figure 4), although the relative intensities change, probably due to a shift in crystal orientation. This is clearly seen in the SEM images of S13\_sheet (Figure 3d), where the flat faces from the crystals are parallel to the sample holder. In the case of S13\_sph&sh\_act, the modification in intensity could also be caused by the break of layered blocks during activation (Figure S2a and b). The SEM appearance of S13\_sheet\_RT and S13\_sheet\_RT\_act (Figure S2c and d) are similar to those of S13\_sheet and S13\_sph&sh\_act owing to the flat arrangement of the particles. Finally, Figure 3 and Figure S2 also show the filler particles (S13\_sph&sh and S13\_sheet\_RT) before and after activation with no evidences of appearance changes.

FTIR spectra of S13\_sheet, S13\_sphere\_1:2, S13\_sphere\_1:1 and S13\_sheet\_RT are displayed in addition to that of S13\_sph&sh in Figure S1. The S13\_sheet and S13\_sheet\_RT spectra, corresponding to samples containing crystals with flat morphology, are in good agreement with that of S13\_sph&sh (sheets and spheres). However, S13\_sphere\_1:2 and S13\_sphere\_1:1 have broad bands at around 1580-1600  $\text{cm}^{-1}$  and between 1438 and 1360  $\text{cm}^{-1}$  (rectangles in Figure S1). According to SEM inspection, the latter samples correspond to spheres. This implies that the composition of the amorphous phase, i.e. spheres, is different from that of S13\_sph&sh. However, the presence of the amorphous phase in S13\_sph&sh is barely perceptible by FTIR analysis, so that a negligible contribution to the properties of S13\_sph&sh would be expected.

Sorption experiments of  $\text{CO}_2$  and  $\text{N}_2$  at low pressure were performed on S13\_sph&sh\_act, S13\_sphere\_1:1\_act and S13\_sheet\_RT\_act (Figures 5a and S3). According to FTIR spectra (Figure S1), the band typical of DMF was not visible for these products, thus they were well-activated. Despite the low BET specific surface areas (5-12  $\text{m}^2 \text{g}^{-1}$ , see Table 1), the  $\text{CO}_2$  adsorption capacities are relatively significant when compared with values from other ZIFs [46-50], especially those of S13\_sph&sh\_act and S13\_sheet\_RT\_act (see Table 1). This is due to the

sheet crystals, whose 2D nature favors selective CO<sub>2</sub> adsorption. S13\_sheet\_RT\_act (0.7 mmol g<sup>-1</sup>) with an uptake similar to that of ZIF-8 almost reached the uptake values of ZIF-97 (1.0 mmol g<sup>-1</sup>) [49] and ZIF-L (0.9 mmol g<sup>-1</sup>) [47]. The latter ZIFs are somewhat similar to UZAR-S13 materials because ZIF-97 (3.08-3.65 Å in aperture size; 16.5 Å in pore diameter) [51] includes in its framework a ligand similar to hmlm (Figure S3) whereas ZIF-L (pore size of 9.4 x 7.0 x 5.3 Å<sup>3</sup>) nanoflakes possess a 2D structure [52]. On the other hand, ZIF-9 (4.31 Å in pore diameter) and ZIF-11 (14.6 Å) do not show N<sub>2</sub> adsorption because their aperture sizes (2.9 and 3.0 Å, respectively) are smaller than the kinetic diameter of N<sub>2</sub> (3.64 Å) [49], but they exhibit structural flexibility due to ligand rotation which allows adsorbates to reach the pores (gate-opening) [53, 54]. The UZAR-S13 type materials adsorb CO<sub>2</sub> but not N<sub>2</sub>. It is supposed that these materials have a pore aperture between the kinetic diameters of CO<sub>2</sub> (3.3 Å) and N<sub>2</sub> in such a way that N<sub>2</sub> molecules cannot reach the pores because they are too large whilst CO<sub>2</sub> fits the pore aperture and is able to enter the pores. Another hypothesis is that the UZAR-S13 materials have a pore aperture below the kinetic diameter of CO<sub>2</sub> and their flexible structure allows the hmlm ligands to rotate upon CO<sub>2</sub> adsorption, thus CO<sub>2</sub> molecules entering the pores, as occurs in ZIF-9 and ZIF-11. The CO<sub>2</sub> adsorption would be enabled in both cases. The ZIFs summarized in Table 1, except ZIF-9 and ZIF-11, show significant BET surface areas because their pore apertures or dimensions exceed the size of the N<sub>2</sub> molecule or, when the pore apertures are slightly lower, because of the mentioned gate-opening effect [53, 54] upon N<sub>2</sub> sorption. The lower CO<sub>2</sub> capacity of S13\_sphere\_1:1\_act arose from its amorphous character, rendering more disordered and less accessible pores. This provoked less CO<sub>2</sub> sorption on S13\_sph&sh\_act, constituted by spheres and sheets, compared to that of S13\_sheet\_RT\_act, formed only by sheets. Therefore, the amorphous contribution to S13\_sph&sh, not noticed by the FTIR studies, was evidenced by CO<sub>2</sub> adsorption.

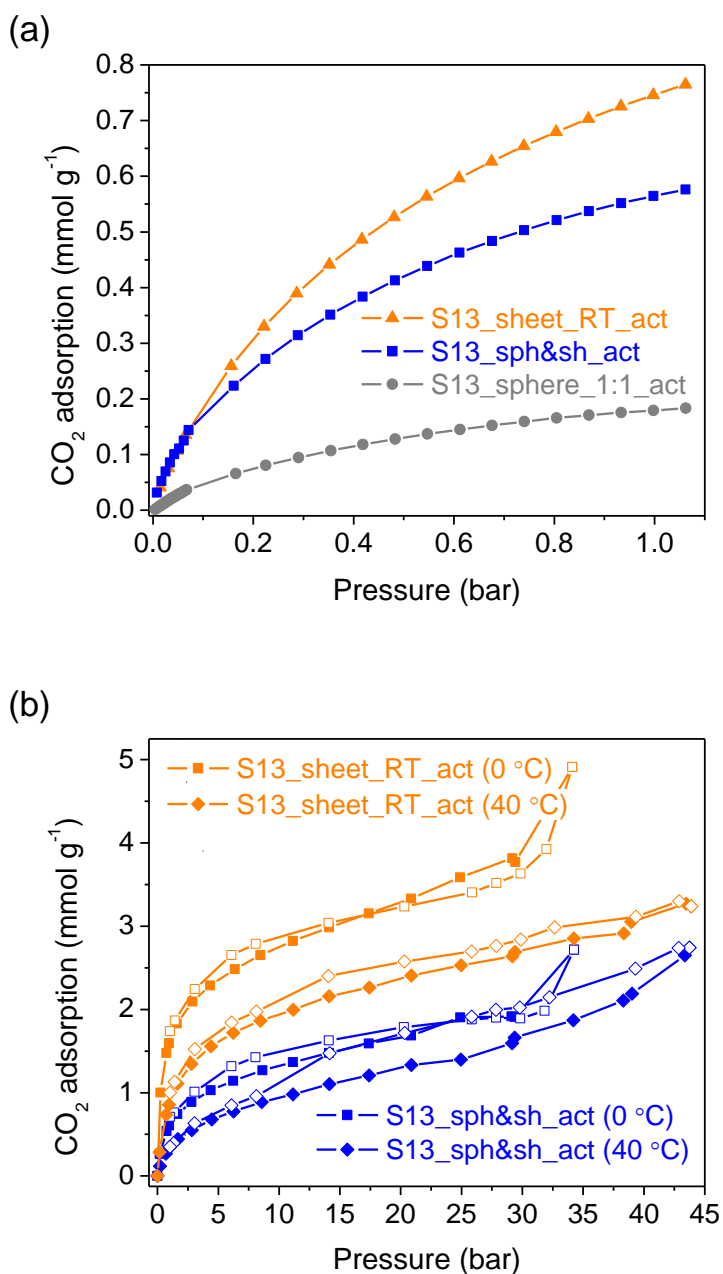


Figure 5. CO<sub>2</sub> adsorption isotherms at (a) low pressure (25 °C) and (b) high pressure (0 and 40 °C) of S13\_sph&sh\_act, S13\_sheet\_RT\_act and S13\_sphere\_1:1\_act (only adsorption at low pressure). High pressure adsorption corresponds to the adsorption excess. Filled and open symbols for adsorption and desorption, respectively.



Table 1. CO<sub>2</sub> adsorption capacities for selected ZIFs

MOF	BET surface area (m <sup>2</sup> g <sup>-1</sup> )	Capacity		P (bar)	T (°C)	Reference
		(mmol g <sup>-1</sup> )	(wt%)			
ZIF-9 (blm)	4	2.7	-	1	0	[54, 55]
ZIF-11 (blm)	-	2.05	-	1.1	0	[53]
ZIF-25 (dmlm)	1110	1.1	-	1	25	[49]
ZIF-71 (dclm)	652	0.6	-	1	25	[49]
ZIF-93 (almlm)	864	1.6	-	1	25	[49]
ZIF-96 (cyamlm)	960	2.1	-	1	25	[49]
ZIF-97 (hymmlm)	564	1.0	-	1	25	[49]
ZIF-L (mlm)	161	0.9	-	1	25	[47]
nZIF-8	1268	-	35.0	30	25	[50]
ZIF-8	1450	0.7	-	1	25	[46]
	1070	<i>ca.</i> 5.9 <sup>a</sup>	-	30	25	[48]
S13_sphere_1:1_act	5	0.2	0.8	1	25	This work
S13_sph&sh_act	12	0.6	2.5	1	25	This work
		1.9	8.4	30	0	
		2.2	9.6	40	40	
S13_sheet_RT_act	8	0.7	3.4	1	25	This work
		3.8	16.6	30	0	
		3.1	13.4	40	40	

<sup>a</sup> Value taken from the CO<sub>2</sub> isotherms of the corresponding reference.

blm, benzimidazole; dmlm: 4,5-dimethylimidazole; dclm: 4,5-dichloroimidazole; almlm: 4-methylimidazole-5-carbaldehyde; cyamlm: 4-aminoimidazole-5-carbonitrile; hymmlm: 4-hydroxymethyl-5-methylimidazole; mlm: 2-methylimidazole.

H<sub>2</sub> physisorption measurements were performed on S13\_sph&sh\_act (Figure S4). H<sub>2</sub> sorption resulted in an uptake of 0.12 wt% at 180 bar, indicating a poor interaction with H<sub>2</sub> molecules. S13\_sph&sh\_act and S13\_sheet\_RT\_act, the more promising materials, were tested for CO<sub>2</sub> sorption at high pressure and two distinct temperatures (0 and 40 °C) (Figure 5b). High pressure isotherms were in good agreement with those obtained at subatmospheric pressures. Most of the CO<sub>2</sub> molecules were adsorbed below 10 bar; above this pressure, the corresponding uptakes were less significant for both temperatures and products.

As we have reported earlier for carbon-based materials [56], mesoporous materials [57], and even ZIFs [53], CO<sub>2</sub> adsorption at high pressures is a very useful technique given that (1) it

enables characterization of narrow porosity (i.e. pores of sizes around 3 Å, which correspond to the narrower cavities found in ZIF-11) and (2) the isotherms are measured up to relative fugacities close to unity [56] at both temperatures (0 and 40 °C), which allows the whole range of porosity to be covered. One interesting feature is that a steep increase in the adsorption capacity is observed for both samples at 0 °C and pressures above 25 bar, which may be ascribed to CO<sub>2</sub> condensation in intercrystalline (or interlamellar) spaces, as we have reported previously [53]. This phenomenon is not observed for sample S13\_sheet\_RT\_act at 40 °C. Adsorption and desorption branches nearly overlap for all the samples except for S13\_sph&sh\_act at 40 °C, which shows a noticeable hysteresis cycle from 43 to 10 bar. This hysteresis cannot be related to capillary condensation since this would only occur in the highest pressure region [53, 56]. It could be due to a strong interaction between the CO<sub>2</sub> molecule and the adsorbent or to a change in size or morphology of the pores at high pressures, trapping the CO<sub>2</sub> in its structure.

As seen in table S2, CO<sub>2</sub> capacities (up to 3.8 mmol g<sup>-1</sup> at 30 bar and 0 °C in the case of S13\_sheet\_RT\_act), even if significant, are below the values for other MOFs. For instance, HKUST-1, containing open metal sites that could enhance CO<sub>2</sub> adsorption [58], adsorbs three times the value of S13\_sheet\_RT\_act. When compared to nZIF-8 and ZIF-8 (Table 1), S13\_sph&sh\_act and S13\_sheet\_RT\_act exhibit between a third and a half, respectively, of CO<sub>2</sub> capacity despite the fact that their BET areas are around 90-160 times smaller. This underlines the great potential of the 2D crystals of ZIFs S13\_sph&sh\_act and S13\_sheet\_RT\_act as CO<sub>2</sub> adsorbents. As in the case of CO<sub>2</sub> adsorption at low pressure, uptakes for S13\_sheet\_RT\_act are higher than those of S13\_sph&sh\_act. This highlights the effect of the amorphous spheres in S13\_sph&sh.

### 3.2 MMM characterization and performance

Following the promising CO<sub>2</sub> adsorption results achieved with S13\_sph&sh and S13\_sheet\_RT, both products were embedded in 6FDA-DAM for MMM fabrication. A ZIF loading of 10 wt% was chosen (even though 20 wt% loading membranes were prepared and tested out of range gas separation performance). The membranes were characterized by SEM, ATR-FTIR and PXRD.

SEM images of the cross section of the MMMs prepared in this work show the ZIF-polymer interaction and the filler distribution in the polymeric matrix (Figure 6). Both S13\_sph&sh and S13\_sheet\_RT are uniformly distributed all over the cross section of the MMMs. Particles of S13\_sph&sh and S13\_sheet\_RT are located in the cavities delimited by the polymeric nerves. Besides, crystals of S13\_sheet\_RT seem to be preferentially oriented parallel to the MMM surface. The insets shown in Figure 6 reveal a good ZIF-polymeric matrix interaction for both S13\_sph&sh and S13\_sheet\_RT.

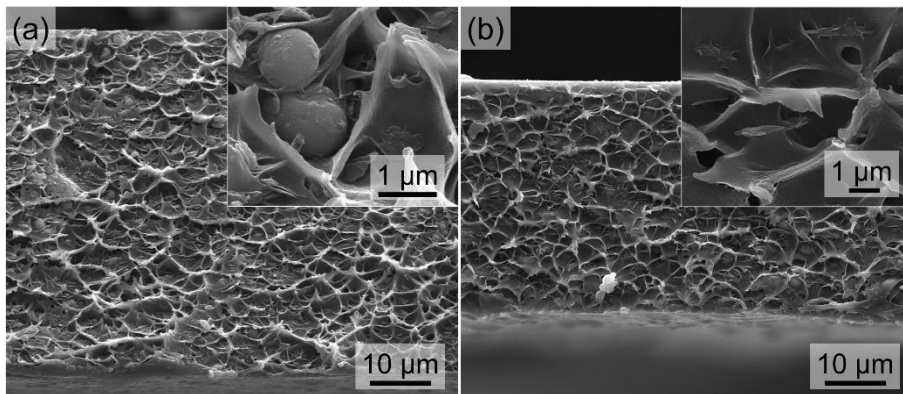


Figure 6. Cross-section SEM images of the MMMs prepared with (a) S13\_sph&sh and (b) S13\_sheet\_RT as fillers.

The ATR-FTIR characterization (Figure S5) shows no difference between the spectra from the bare membrane and the two MMMs. Only bands related to 6FDA-DAM are seen. This is due to the low ZIF loading of the MMMs (10 wt%).

The thermogram of the neat 6FDA-DAM membrane show a weight loss of 2.8 % below 75 °C, attributed to the removal of water molecules adsorbed from the atmosphere (Figure S6). The small decreasing trend (0.6 %) from 75 °C to degradation (around 380 °C) corresponds to chloroform release. This low percentage indicates that the neat membrane was successfully activated. The weight loss of 0.8 and 1.5 % between 25-125 °C for S13\_sph&sh/6FDA-DAM and S13\_sheet\_RT/6FDA-DAM MMMs is probably due to chloroform and water removal. These insignificant values confirm the success in activating the MMMs. The step at 125-285 °C for both membranes (1.2 and 1.4 %, respectively) is ascribed to the filler presence. The decomposition of the MMMs takes place above 380 °C, as that of the bare polymer. DSC experiments were carried out to determine the  $T_g$  of the distinct membranes (Table 2). The bare 6FDA-DAM shows a  $T_g$  within the reported values for the same polymer (Table S3). As seen, the  $T_g$  rises from 384.1 °C for the pure polymer to 400.2 and 399.9 °C for S13\_sph&sh/6FDA-DAM and S13\_sheet\_RT/6FDA-DAM, respectively. As expected, the glass transition temperatures for S13\_sph&sh and S13\_sheet\_RT are similar because both fillers share the same nature. The increase in  $T_g$  (about 16 °C) was caused by the rigidification of the polymer, i.e. the movement of the polymer chains surrounding the filler particles was restricted because of chemical interactions between both components [59, 60]. The calculated  $T_g$  could show the effect of the corresponding decomposed fillers.

Table 2. Glass transition temperatures and d-spacings (calculated by Bragg's law) for the membranes prepared in this work

Membrane	T <sub>g</sub> (°C)	d-spacing (Å)
Bare 6FDA-DAM	384.1	7.0
S13_sph&sh/6FDA-DAM	400.2	6.3
S13_sheet_RT/6FDA-DAM	399.9	6.4

X-ray diffractometry revealed amorphous and broad bands centred at the  $2\theta$  values of  $13.6^\circ$  and  $13.8^\circ$  for the S13\_sph&sh/6FDA-DAM and S13\_sheet\_RT/6FDA-DAM MMMs, respectively (Figure S7). The displacement of the amorphous band from the bare 6FDA-DAM ( $2\theta = 12.7^\circ$ ) towards higher  $2\theta$  angles involves a decrease in the d-spacing ( $7.0 \text{ \AA}$  vs.  $6.3$  and  $6.4 \text{ \AA}$ , see Table 2). Because of the similarity of the fillers, the corresponding d-spacings barely differ. The d-spacing is related to the interchain distance [61], giving an indication of the packing density of the polymer chains [59]. Thus, lower d-spacings imply a strong filler-polymer interaction which would reduce the distance between the polymeric chains [62]. However, the lower d-spacing could hamper the diffusion of small molecules through the membranes, producing lower permeabilities [59, 61]. The d-spacing for the pure 6FDA-DAM membrane is somewhat higher than the values found in the literature (Table S3). The reflection at  $2\theta = 14.4^\circ$  of the S13\_sheet\_RT/6FDA-DAM membrane is related to the strong peak at  $2\theta = 14.1^\circ$  from the filler, corroborating the preservation of its crystallinity. In addition, some parallel preferential orientation of the filler sheets to the membrane itself may provoke the disappearance of certain minor intensities, as observed for other MMMs with lamellar fillers [63]. In the case of the S13\_sph&sh/6FDA-DAM membrane, a weak signal at  $2\theta = 8.6^\circ$  is ascribed to S13\_sph&sh ( $2\theta = 8.7^\circ$ ). The filler-polymer interaction caused changes in the crystal lattice of S13\_sph&sh and S13\_sheet\_RT, producing these shifts in the peak positions to lower or higher angles.

As mentioned in the Experimental section, the activation of the UZAR-S13 materials was carried out by a solvent-exchange process for 7 d with anhydrous chloroform and a

subsequent vacuum treatment at 80 °C for 8 h. Nonetheless, the activation of the MMMs was performed at 100 °C for 1 d without vacuum. In order to confirm that the fillers supported the conditions used in the activation of the membranes, a sample of S13\_sph&sh was soaked in anhydrous chloroform for 7 d and was then treated at 100 °C for 1 d (S13\_sph&sh\_100°C). The PXRD pattern, FTIR spectrum and SEM images of S13\_sph&sh\_100°C are shown in Figure S8, Figure S9 and Figure S2 (e and f), respectively. The FTIR spectrum agrees with that of S13\_sph&sh\_act and the particle morphologies of both samples were similar. The higher difference was found by PXRD. S13\_sph&sh\_act and S13\_sph&sh\_100°C share the same structure, but the peaks of S13\_sph&sh\_100°C are broader and less defined. Thus, the activation of the MMMs might have damaged slightly the structure of the fillers.

Given the affinity of the fillers towards CO<sub>2</sub>, the S13\_sph&sh/6FDA-DAM and S13\_sheet\_RT/6FDA-DAM MMMs were applied to separate several CO<sub>2</sub> containing mixtures typical of post-combustion, pre-combustion and natural gas purification processes: CO<sub>2</sub>/N<sub>2</sub>, CO<sub>2</sub>/H<sub>2</sub> and CO<sub>2</sub>/CH<sub>4</sub>, respectively. The 6FDA-DAM polymer is highly permeable, especially towards CO<sub>2</sub>. This could affect significantly the permeation results [64].

The distinct sorption studies carried out (described above) could help to understand the gas separation results. Four facts are concluded from the H<sub>2</sub>, CO<sub>2</sub> and N<sub>2</sub> sorption. (1) N<sub>2</sub> molecules are unable to enter into the pores of S13\_sph&sh and S13\_sheet\_RT because the kinetic diameter of N<sub>2</sub> is bigger than the pore aperture of the fillers. (2) The interactions between H<sub>2</sub> molecules and the pore walls of S13\_sph&sh and S13\_sheet\_RT are weak. (3) The pores of the 2D crystals in both fillers have a noticeable affinity towards CO<sub>2</sub>. (4) As S13\_sheet\_RT does not contain amorphous spherical particles, its CO<sub>2</sub> uptake is higher.

Permeability and selectivity data are depicted in Figure 7 and Table S4. The permeabilities of H<sub>2</sub>, CH<sub>4</sub> and N<sub>2</sub> for the bare 6FDA-DAM match well with those reported in the literature [59, 65], although the permeability of CO<sub>2</sub> (1237-1289 Barrer) is around twofold in comparison with

the value obtained by Zornoza *et al.* (mixed gas permeability, 604-681 Barrer) [65] and 1.5-fold with respect to that reported by Qiu *et al.* (single gas permeability, 842 Barrer) [59]. In contrast, the results presented by Boroglu and Yumru [61] and Kim *et al.* [66] ( $\text{CO}_2$  single gas permeabilities of 20.6 and 299 Barrer, respectively) are much lower than the values obtained here.

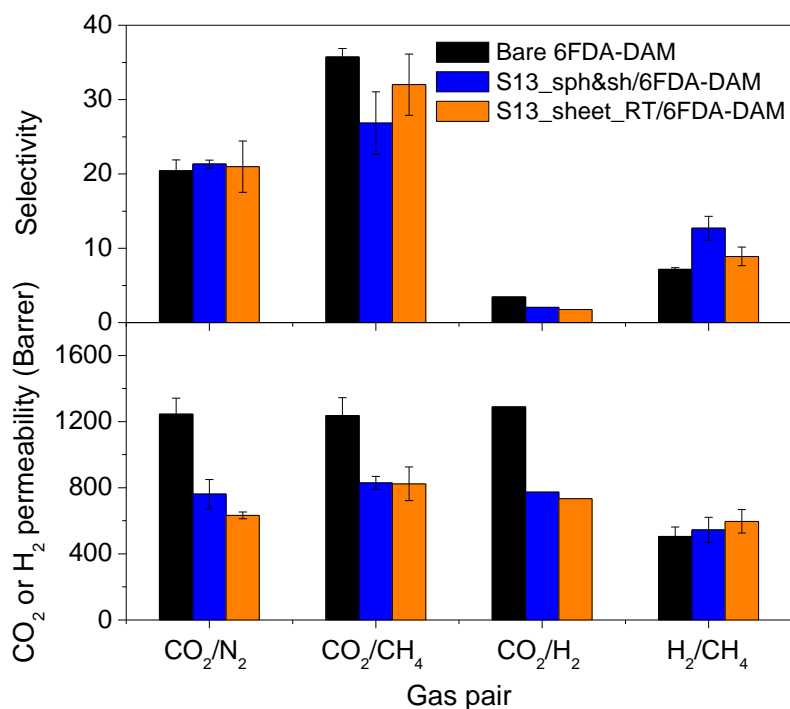


Figure 7. Permeability and selectivity results for the bare 6FDA-DAM membrane, S13\_sph&sh/6FDA-DAM and S13\_sheet\_RT/6FDA-DAM. Error bars indicate the standard deviation of at least two membranes.

Figure 7 shows that the permeabilities of  $\text{CO}_2$ ,  $\text{N}_2$  and  $\text{CH}_4$  decreased as compared to that of the neat polymer for the three gas pairs whereas only the permeability of  $\text{H}_2$  increased (see also Table S4). These reductions (for all the gases except  $\text{H}_2$ ) suggest that the MMMs are defect-free without interface voids, indicating a good polymer-filler contact, as observed by SEM (Figure 6). Interface voids would cause a large increase in permeability for all the gases and non-selective flows [67, 68].

There are five main explanations for the decrease in permeability. (1) As stated above, 6FDA-DAM is highly permeable to gases, especially to CO<sub>2</sub>, so that the use of less permeable fillers would lead to lower gas permeabilities through the MMMs. (2) A higher tortuosity due to the filler presence in the polymeric matrix disturbs the gas diffusion, increasing the pathlength through the MMMs [69]. (3) Rigidification limits the mobility of the polymer chains around the filler particles (at the polymer-filler interface) in comparison to that of the pure polymer [68]. Rigidification only affects a very thin coating of polymer surrounding the filler particles so that permeability does not decrease significantly [68] (the thickness of the rigidified polymer region near the porous particles of zeolite 4A and carbon molecular sieves dispersed in different polymeric matrices have been assumed to be between 2.5 and 20 % of the particle size) [70-73]. This phenomenon also provokes an increase in the gas separation performance because the lower mobility of the polymer chains improves the diffusivity selectivity [68]. (4) Pore blocking by the polymer chains may narrow the pore size of the fillers. Polymer chains are able to fill the pores in various degrees depending on the pore size, restricting the gas passing through the membranes [61, 68]. Even small pores (a few Å in pore diameter) could be affected by this phenomenon, as observed by Li *et al.* [70]. They prepared MMMs with polyethersulfone (PES) as the polymer matrix and zeolite 3A, 4A and 5A as fillers to separate an O<sub>2</sub>/N<sub>2</sub> mixture (the kinetic diameter of O<sub>2</sub> is 3.5 Å). It was found that the blocking narrowed the pore of zeolite 5A (4.5 Å) down to *ca.* 4 Å, improving the separation performance [70]. The blocking effect was also demonstrated for zeolite 3A (3 Å) and 4A (3.8 Å); their pores were partially blocked by the PES chains, resulting in a higher resistance to the O<sub>2</sub> transport [70]. Pore blocking is generally accompanied by rigidification (in agreement with the T<sub>g</sub> values shown above) and its effect on selectivity depends on the original pore size of the fillers [68]. (5) The clogged sieve occurs when pores are totally blocked by strongly adsorbed molecules (e.g. gas penetrant or solvent coming from the membrane preparation) [74]. The selectivity barely differs although permeability decreases for all the penetrants.



The reduction in the permeability of CO<sub>2</sub> in these gas mixtures ranges between 33 and 50 % for both MMMs. The corresponding values for N<sub>2</sub> and CH<sub>4</sub> are found within 40-50 % and 10-25 %, respectively. These high percentages suggest pore blocking rather than rigidification. The pore blocking is thought to have narrowed the pore size of both fillers in the MMMs below the kinetic diameter of CO<sub>2</sub> in such a way that the flow of CO<sub>2</sub>, CH<sub>4</sub> and N<sub>2</sub> molecules was impeded by a molecular sieving effect and only H<sub>2</sub> was capable of diffusing faster.

As observed in Table S4, the permeabilities of CO<sub>2</sub>, N<sub>2</sub> and CH<sub>4</sub> through S13\_sph&sh/6FDA-DAM are greater than those through S13\_sheet\_RT/6FDA-DAM while the value for H<sub>2</sub> is smaller in the case of S13\_sph&sh/6FDA-DAM. The amorphous component of S13\_sph&sh contributes disordered pores which would hamper the gas flux through S13\_sph&sh/6FDA-DAM. Thus a lower permeability of all the gases would be expected through the S13\_sph&sh/6FDA-DAM membrane. Also, a higher permeability of CO<sub>2</sub> for S13\_sheet\_RT/6FDA-DAM than that of S13\_sph&sh/6FDA-DAM would be expected because of the higher affinity of S13\_sheet\_RT (having only sheet crystals and not the amorphous spheres). It is thought that the strong CO<sub>2</sub> adsorption on the pore walls of S13\_sheet\_RT and the CO<sub>2</sub>-CO<sub>2</sub> interactions could hinder the flux through the S13\_sheet\_RT/6FDA-DAM MMM, obtaining a lower value of permeability in comparison to that of S13\_sph&sh/6FDA-DAM which is filled with less CO<sub>2</sub> adsorbent particles (spheres and sheets). This phenomenon also affects the gas flow of the bulkier CH<sub>4</sub> and N<sub>2</sub> molecules, so that the corresponding permeabilities are lower for the S13\_sheet\_RT/6FDA-DAM membrane. In fact, the permeability of N<sub>2</sub> was reduced by 42 and 50 % for S13\_sph&sh/6FDA-DAM and S13\_sheet\_RT/6FDA-DAM, whereas that of CH<sub>4</sub> fell by 10 and 25 %, respectively, confirming the CO<sub>2</sub> adsorption effect also on the N<sub>2</sub> and CH<sub>4</sub> fluxes through S13\_sheet\_RT/6FDA-DAM. The orientation in the MMM of the sheet crystals of S13\_sheet\_RT, parallel to the surface (Figure 6b), increases the barrier effect towards CO<sub>2</sub>, N<sub>2</sub> and CH<sub>4</sub> due to the higher tortuosity. The flow of H<sub>2</sub> is less affected by the CO<sub>2</sub> adsorption phenomenon due to its smaller kinetic

diameter. Because of this and the fact that S13\_sheet\_RT/6FDA-DAM does not contain amorphous particles, the H<sub>2</sub> molecules pass faster through this MMM.

As mentioned above, the 6FDA-DAM polymer is known for its high capacity to promote a high permeability of CO<sub>2</sub> with moderate selectivity [64]. In fact, it is more permeable to CO<sub>2</sub> than to H<sub>2</sub>, as can be seen in Figure 7, giving an inverse H<sub>2</sub>/CO<sub>2</sub> selectivity. Regarding the CO<sub>2</sub>/H<sub>2</sub> mixture (Figure 7 and Table S4), a decrease in the selectivity is observed compared to that of the pure polymer. This is as expected since the permeability of CO<sub>2</sub> is lower while the permeability of H<sub>2</sub> increases for both MMMs. Considering the other gas mixtures (Figure 7 and Table S4), while the CO<sub>2</sub>/N<sub>2</sub> selectivity for the MMMs slightly exceeds that of the bare polymer, the CO<sub>2</sub>/CH<sub>4</sub> selectivity falls. As the CH<sub>4</sub> molecule is bigger than the N<sub>2</sub> molecule, a greater limitation on the flux of CH<sub>4</sub> would be expected, enhancing the CO<sub>2</sub>/CH<sub>4</sub> selectivity. The inclusion of particles of S13\_sph&sh and S13\_sheet\_RT in the polymeric matrix may lead to an improvement in the solubility of the more condensable gas (-162 and -196 °C for CH<sub>4</sub> and N<sub>2</sub>) and thus a larger permeability of CH<sub>4</sub> than expected. This is due to the morphology changes at the polymer-filler interface which facilitate the solution of the more condensable gases in the MMM [69]. It is worth noting that the improvement in solubility is more significant for S13\_sheet\_RT since this filler is more crystalline.

The MMMs act as molecular sieves for the H<sub>2</sub>/CH<sub>4</sub> mixture, separating both gas components by size exclusion (Figure 7 and Table S4), as seen with narrow porosity fillers such as titanosilicate JFD-L1 [63] and exfoliated zeolite Nu-6(2) [75] in analogous 6FDA-based copolyimides. The H<sub>2</sub> molecules are able to enter the filler pores and permeate through them whereas the CH<sub>4</sub> molecules are too large to enter the pores and remain at the retentate side. The permeabilities of H<sub>2</sub> and CH<sub>4</sub> are thus higher and lower, respectively, through the MMMs than those through the bare 6FDA-DAM. The permeability of both gases is smaller for S13\_sph&sh/6FDA-DAM because the amorphous character of S13\_sph&sh hinders the gas flow through its pores, as

mentioned above. In consequence, the MMMs increase the H<sub>2</sub>/CH<sub>4</sub> selectivity (Figure 7), and the selectivity of S13\_sph&sh/6FDA-DAM is higher. This is because the flow of CH<sub>4</sub> decreases by 39 and 5 % while that of H<sub>2</sub> increases by 8 and 18 % for S13\_sph&sh/6FDA-DAM and S13\_sheet\_RT/6FDA-DAM, respectively. The presence of the amorphous spherical particles in the filler of S13\_sph&sh/6FDA-DAM constitutes a greater hurdle to the CH<sub>4</sub> molecules, counteracting the lower increase in the flux of H<sub>2</sub>. The selectivity is increased 1.8-fold by S13\_sph&sh/6FDA-DAM (12.7) and 1.2-fold by S13\_sheet\_RT/6FDA-DAM (8.9) compared to the neat membrane (7.2). These results suggest that S13\_sph&sh is a potential candidate for incorporation into MMMs for H<sub>2</sub>/CH<sub>4</sub> separation while S13\_sheet\_RT could be embedded into a different polymeric matrix to promote the separation of H<sub>2</sub> from CO<sub>2</sub> by a barrier effect.

#### 4 Conclusions

The synthesis of a new ZIF based on hydroxymethylimidazolate, UZAR-S13 (S13\_sph&sh), is reported. In the UZAR-S13 skeleton, Zn<sup>2+</sup> ions act as nodes while hmIm linkers are the struts that connect nodes through coordination bonds. Morphology and X-ray diffractometry studies revealed that UZAR-S13 contains two distinct phases: amorphous spheres and crystalline sheets. Increasing or diminishing the metal:ligand ratio led respectively to obtaining spheres or sheets only. Flat particles were also obtained when the reaction time and temperature changed. Thus, the reaction parameters had a direct influence on the morphology and presence of amorphous phases, demonstrating that small experimental adjustments could result in the desired product. In spite of their low BET specific surface areas, several UZAR-S13-type materials presented good CO<sub>2</sub> uptakes at low pressures, approaching the uptakes of ZIFs with BET areas about 50 times higher, and notable values at high pressures. Both products were included as fillers in MMMs, where their sheet-shaped crystals could provide benefits in gas separation performance. Four distinct separations were studied (CO<sub>2</sub>/N<sub>2</sub>, CO<sub>2</sub>/CH<sub>4</sub>, CO<sub>2</sub>/H<sub>2</sub> and H<sub>2</sub>/CH<sub>4</sub>). The results for the mixtures containing CO<sub>2</sub> demonstrated that the 2D crystals of

S13\_sph&sh and S13\_sheet\_RT established strong interactions with the CO<sub>2</sub> molecules, hampering the flow of CO<sub>2</sub>, N<sub>2</sub> and CH<sub>4</sub> through the MMMs. This barrier effect was increased by the arrangement of the crystals parallel to the membrane surface, as demonstrated by PXRD and SEM characterization. The decrease in permeability of CO<sub>2</sub>, N<sub>2</sub> and CH<sub>4</sub> through S13\_sph&sh/6FDA-DAM and S13\_sheet\_RT/6FDA-DAM was also due to pore blocking by the polymeric chains which narrowed the pore size of both fillers, the smallest H<sub>2</sub> molecule being less affected. Neither UZAR-S13 nor S13\_sheet\_RT improved the performance of the bare 6FDA-DAM membrane for CO<sub>2</sub> containing mixtures. For the H<sub>2</sub>/CH<sub>4</sub> pair, the fillers provoked an increase in the selectivity by a molecular sieving effect with a greater improvement for S13\_sph&sh/6FDA-DAM. The amorphous spherical particles of S13\_sph&sh restricted the flux of CH<sub>4</sub> to a higher degree, counteracting the lower increase in the flow of H<sub>2</sub> in comparison to that of S13\_sheet\_RT/6FDA-DAM. UZAR-S13 materials are capable of distinguishing molecules with different kinetic diameters and show strong interaction with CO<sub>2</sub> molecules, allowing their use in membrane-based gas separations.

### **Acknowledgements**

Financial support from the Spanish Ministry of Economy and Competitiveness (MINECO) and FEDER (MAT2013-40556-R, MAT2016-77290-R (MINECO/FEDER) and CTQ2015-66080-R (MINECO/FEDER)), the European Social Fund (ESF) and the Aragón Government (DGA, T05) is gratefully acknowledged. A. P.-C. and J. S.-L. also thank the DGA and MINECO, respectively, for Ph.D. grants. The microscopy work was carried out in the Laboratorio de Microscopías Avanzadas at the Instituto de Nanociencia de Aragón (LMA-INA, Universidad de Zaragoza). The authors would like to acknowledge the use of the Servicio General de Apoyo a la Investigación-SAI (Universidad de Zaragoza).

## References

- [1] R. Sabouni, H. Kazemian, S. Rohani, Carbon dioxide capturing technologies: a review focusing on metal organic framework materials (MOFs), *Environ. Sci. Pollut. Res.* 21 (2014) 5427-5449.
- [2] Y. Liu, Z.U. Wang, H.-C. Zhou, Recent advances in carbon dioxide capture with metal-organic frameworks, *Greenhouse Gases: Sci. Technol.* 2 (2012) 239-259.
- [3] K. Sumida, D.L. Rogow, J.A. Mason, T.M. McDonald, E.D. Bloch, Z.R. Herm, T.-H. Bae, J.R. Long, Carbon dioxide capture in metal-organic frameworks, *Chem. Rev.* 112 (2012) 724-781.
- [4] P. Serra-Crespo, R. Berger, W. Yang, J. Gascon, F. Kapteijn, Separation of CO<sub>2</sub>/CH<sub>4</sub> mixtures over NH<sub>2</sub>-MIL-53-An experimental and modelling study, *Chem. Eng. Sci.* 124 (2015) 96-108.
- [5] X. Wu, M.N. Shahrak, B. Yuan, S. Deng, Synthesis and characterization of zeolitic imidazolate framework ZIF-7 for CO<sub>2</sub> and CH<sub>4</sub> separation, *Microporous Mesoporous Mater.* 190 (2014) 189-196.
- [6] K.V. Kumar, G. Charalambopoulou, M. Kainourgiakis, A. Stubos, T. Steriotis, Insights on the physical adsorption of hydrogen and methane in UiO series of MOFs using molecular simulations, *Comput. Theor. Chemistry* 1061 (2015) 36-45.
- [7] C.M. Simon, J. Kim, L.-C. Lin, R.L. Martin, M. Haranczyk, B. Smit, Optimizing nanoporous materials for gas storage, *Phys. Chem. Chem. Phys.* 16 (2014) 5499-5513.
- [8] J.-R. Li, J. Sculley, H.-C. Zhou, Metal-organic frameworks for separations, *Chem. Rev.* 112 (2012) 869-932.
- [9] S.R. Venna, M.A. Carreon, Metal-organic framework membranes for carbon dioxide separation, *Chem. Eng. Sci.* 124 (2015) 3-19.

- [10] M. Shah, M.C. McCarthy, S. Sachdeva, A.K. Lee, H.-K. Jeong, Current status of metal-organic framework membranes for gas separations: promises and challenges, *Ind. Eng. Chem. Res.* 51 (2012) 2179-2199.
- [11] B. Zornoza, C. Tellez, J. Coronas, J. Gascon, F. Kapteijn, Metal-organic framework based mixed matrix membranes: an increasingly important field of research with a large application potential, *Microporous Mesoporous Mater.* 166 (2013) 67-78.
- [12] S. Japip, H. Wang, Y.C. Xiao, T.S. Chung, Highly permeable zeolitic imidazolate framework (ZIF)-71 nano-particles enhanced polyimide membranes for gas separation, *J. Membr. Sci.* 467 (2014) 162-174.
- [13] S. Japip, K.S. Liao, T.S. Chung, Molecularly tuned free volume of vapor cross-linked 6FDA-durene/ZIF-71 MMMs for H<sub>2</sub>/CO<sub>2</sub> separation at 150 °C, *Adv. Mater.* 29 (2017).
- [14] P. Amo-Ochoa, F. Zamora, Coordination polymers with nucleobases: from structural aspects to potential applications, *Coord. Chem. Rev.* 276 (2014) 34-58.
- [15] S. Kitagawa, R. Kitaura, S. Noro, Functional porous coordination polymers, *Angew. Chem., Int. Ed.* 43 (2004) 2334-2375.
- [16] S.L. Qiu, G.S. Zhu, Molecular engineering for synthesizing novel structures of metal-organic frameworks with multifunctional properties, *Coord. Chem. Rev.* 253 (2009) 2891-2911.
- [17] C. Serre, F. Millange, C. Thouvenot, M. Nogues, G. Marsolier, D. Louer, G. Ferey, Very large breathing effect in the first nanoporous chromium(III)-based solids: MIL-53 or Cr<sup>III</sup>(OH)·{O<sub>2</sub>C-C<sub>6</sub>H<sub>4</sub>-CO<sub>2</sub>}·{HO<sub>2</sub>C-C<sub>6</sub>H<sub>4</sub>-CO<sub>2</sub>H}<sub>x</sub>·H<sub>2</sub>O<sub>y</sub>, *J. Am. Chem. Soc.* 124 (2002) 13519-13526.
- [18] K.S. Park, Z. Ni, A.P. Cote, J.Y. Choi, R.D. Huang, F.J. Uribe-Romo, H.K. Chae, M. O'Keeffe, O.M. Yaghi, Exceptional chemical and thermal stability of zeolitic imidazolate frameworks, *Proc. Natl. Acad. Sci. U. S. A.* 103 (2006) 10186-10191.

- [19] B. Chen, Z. Yang, Y. Zhu, Y. Xia, Zeolitic imidazolate framework materials: recent progress in synthesis and applications, *J. Mater. Chem. A* 2 (2014) 16811-16831.
- [20] S.R. Venna, J.B. Jasinski, M.A. Carreon, Structural evolution of zeolitic imidazolate framework-8, *J. Am. Chem. Soc.* 132 (2010) 18030-18033.
- [21] J. Cravillon, R. Nayuk, S. Springer, A. Feldhoff, K. Huber, M. Wiebcke, Controlling zeolitic imidazolate framework nano- and microcrystal formation: insight into crystal growth by time-resolved in situ static light scattering, *Chem. Mater.* 23 (2011) 2130-2141.
- [22] G. Yilmaz, A. Ozcan, S. Keskin, Computational screening of ZIFs for CO<sub>2</sub> separations, *Mol. Sim.* 41 (2015) 713-726.
- [23] A. Phan, C.J. Doonan, F.J. Uribe-Romo, C.B. Knobler, M. O'Keeffe, O.M. Yaghi, Synthesis, structure, and carbon dioxide capture properties of zeolitic imidazolate frameworks, *Acc. Chem. Res.* 43 (2010) 58-67.
- [24] S. Wang, Q. Yang, J. Zhang, X. Zhang, C. Zhao, L. Jiang, C.-Y. Su, Two-dimensional charge-separated metal-organic framework for hysteretic and modulated sorption, *Inorg. Chem.* 52 (2013) 4198-4204.
- [25] S.C. Junggeburth, L. Diehl, S. Werner, V. Duppel, W. Sigle, B.V. Lotsch, Ultrathin 2D coordination polymer nanosheets by surfactant-mediated synthesis, *J. Am. Chem. Soc.* 135 (2013) 6157-6164.
- [26] A.A. Balandin, Thermal properties of graphene and nanostructured carbon materials, *Nat. Mater.* 10 (2011) 569-581.
- [27] J.N. Coleman, M. Lotya, A. O'Neill, S.D. Bergin, P.J. King, U. Khan, K. Young, A. Gaucher, S. De, R.J. Smith, I.V. Shvets, S.K. Arora, G. Stanton, H.Y. Kim, K. Lee, G.T. Kim, G.S. Duesberg, T. Hallam, J.J. Boland, J.J. Wang, J.F. Donegan, J.C. Grunlan, G. Moriarty, A. Shmeliov, R.J. Nicholls, J.M. Perkins, E.M. Grieveson, K. Theuvsissen, D.W. McComb, P.D. Nellist, V. Nicolosi, Two-dimensional nanosheets produced by liquid exfoliation of layered materials, *Science* 331 (2011) 568-571.

- [28] T.E. Mallouk, J.A. Gavin, Molecular recognition in lamellar solids and thin films, *Acc. Chem. Res.* 31 (1998) 209-217.
- [29] T. Rodenas, I. Luz, G. Prieto, B. Seoane, H. Miro, A. Corma, F. Kapteijn, F.X. Llabres i Xamena, J. Gascon, Metal-organic framework nanosheets in polymer composite materials for gas separation, *Nat. Mater.* 14 (2015) 48-55.
- [30] W. Wang, J.-Y. Sun, D.-J. Zhang, T.-Y. Song, W. Song, L.-Y. Zhang, Y.-L. Chen, Y. Fan, P. Zhang, New two-dimensional metal-organic frameworks constructed from 1H-benzimidazole-5,6-dicarboxylic acid with luminescent studies, *Inorg. Chim. Acta* 384 (2012) 105-110.
- [31] C. Rubio, B. Zornoza, P. Gorgojo, C. Tellez, J. Coronas, Separation of H<sub>2</sub> and CO<sub>2</sub> containing mixtures with mixed matrix membranes based on layered materials, *Curr. Org. Chem.* 18 (2014) 2351-2363.
- [32] K. Varoon, X. Zhang, B. Elyassi, D.D. Brewer, M. Gettel, S. Kumar, J.A. Lee, S. Maheshwari, A. Mittal, C.-Y. Sung, M. Cococcioni, L.F. Francis, A.V. McCormick, K.A. Mkhoyan, M. Tsapatsis, Dispersible exfoliated zeolite nanosheets and their application as a selective membrane, *Science* 334 (2011) 72-75.
- [33] K. Nakagawa, D. Tanaka, S. Horike, S. Shimomura, M. Higuchi, S. Kitagawa, Enhanced selectivity of CO<sub>2</sub> from a ternary gas mixture in an interdigitated porous framework, *Chem. Commun.* 46 (2010) 4258-4260.
- [34] A. Perea-Cachero, B. Seoane, B. Diosdado, C. Tellez, J. Coronas, Synthesis, structure and characterization of a layered coordination polymer based on Zn(II) and 6-(methylmercapto)purine, *RSC Adv.* 6 (2016) 260-268.
- [35] Y. Inubushi, S. Horike, T. Fukushima, G. Akiyama, R. Matsuda, S. Kitagawa, Modification of flexible part in Cu<sup>2+</sup> interdigitated framework for CH<sub>4</sub>/CO<sub>2</sub> separation, *Chem. Commun.* 46 (2010) 9229-9231.



- [36] Y. Peng, Y. Li, Y. Ban, H. Jin, W. Jiao, X. Liu, W. Yang, Metal-organic framework nanosheets as building blocks for molecular sieving membranes, *Science* 346 (2014) 1356-1359.
- [37] D. Andirova, C.F. Cogswell, Y. Lei, S. Choi, Effect of the structural constituents of metal-organic frameworks on carbon dioxide capture, *Microporous Mesoporous Mater.* 219 (2016) 276-305.
- [38] L. Wang, Y.M. Cao, M.Q. Zhou, S.J. Zhou, Q. Yuan, Novel copolyimide membranes for gas separation, *J. Membr. Sci.* 305 (2007) 338-346.
- [39] J.H. Kim, S.B. Lee, S.Y. Kim, Incorporation effects of fluorinated side groups into polyimide membranes on their physical and gas permeation properties, *J. Appl. Polym. Sci.* 77 (2000) 2756-2767.
- [40] C.A. Schneider, W.S. Rasband, K.W. Eliceiri, NIH Image to ImageJ: 25 years of image analysis, *Nat. Methods* 9 (2012) 671-675.
- [41] C. Zhang, X.S. Lu, A.Z. Gu, How to accurately determine the uptake of hydrogen in carbonaceous materials, *Int. J. Hydrogen Energy* 29 (2004) 1271-1276.
- [42] T. Kiyobayashi, H.T. Takeshita, H. Tanaka, N. Takeichi, A. Zuttel, L. Schlapbach, N. Kuriyama, Hydrogen adsorption in carbonaceous materials: how to determine the storage capacity accurately, *J. Alloys Compd.* 330 (2002) 666-669.
- [43] R. Banerjee, A. Phan, B. Wang, C. Knobler, H. Furukawa, M. O'Keeffe, O.M. Yaghi, High-throughput synthesis of zeolitic imidazolate frameworks and application to CO<sub>2</sub> capture, *Science* 319 (2008) 939-943.
- [44] S. Bhattacharjee, M.-S. Jang, H.-J. Kwon, W.-S. Ahn, Zeolitic imidazolate frameworks: synthesis, functionalization, and catalytic/adsorption applications, *Catal. Surv. Asia* 18 (2014) 101-127.
- [45] A. Schaate, M. Schulte, M. Wiebcke, A. Godt, P. Behrens, One-dimensional Zn(II) oligo(phenyleneethynylene)dicarboxylate coordination polymers: synthesis, crystal

- structures, thermal and photoluminescent properties, *Inorg. Chim. Acta* 362 (2009) 3600-3606.
- [46] C. Chen, J. Kim, D.-A. Yang, W.-S. Ahn, Carbon dioxide adsorption over zeolite-like metal organic frameworks (ZMOFs) having a sod topology: structure and ion-exchange effect, *Chem. Eng. J.* 168 (2011) 1134-1139.
- [47] R. Chen, J. Yao, Q. Gu, S. Smeets, C. Baerlocher, H. Gu, D. Zhu, W. Morris, O.M. Yaghi, H. Wang, A two-dimensional zeolitic imidazolate framework with a cushion-shaped cavity for CO<sub>2</sub> adsorption, *Chem. Commun.* 49 (2013) 9500-9502.
- [48] D.F. Liu, Y.B. Wu, Q.B. Xia, Z. Li, H.X. Xi, Experimental and molecular simulation studies of CO<sub>2</sub> adsorption on zeolitic imidazolate frameworks: ZIF-8 and amine-modified ZIF-8, *Adsorption* 19 (2013) 25-37.
- [49] W. Morris, B. Leung, H. Furukawa, O.K. Yaghi, N. He, H. Hayashi, Y. Houndonougbo, M. Asta, B.B. Laird, O.M. Yaghi, A combined experimental-computational investigation of carbon dioxide capture in a series of isorecticular zeolitic imidazolate frameworks, *J. Am. Chem. Soc.* 132 (2010) 11006-11008.
- [50] S.K. Nune, P.K. Thallapally, A. Dohnalkova, C. Wang, J. Liu, G.J. Exarhos, Synthesis and properties of nano zeolitic imidazolate frameworks, *Chem. Commun.* 46 (2010) 4878-4880.
- [51] K.G. Ray, D.L. Olmsted, J.M.R. Burton, Y. Houndonougbo, B.B. Laird, M. Asta, Gas membrane selectivity enabled by zeolitic imidazolate framework electrostatics, *Chem. Mater.* 26 (2014) 3976-3985.
- [52] Y. Lo, C.H. Lam, C.W. Chang, A.C. Yang, D.Y. Kang, Polymorphism/pseudopolymorphism of metal-organic frameworks composed of zinc(II) and 2methylimidazole: synthesis, stability, and application in gas storage, *RSC Adv.* 6 (2016) 89148-89156.
- [53] J. Sanchez-Lainez, B. Zornoza, A. Mayoral, A. Berenguer-Murcia, D. Cazorla-Amoros, C. Tellez, J. Coronas, Beyond the H<sub>2</sub>/CO<sub>2</sub> upper bound: one-step crystallization and

- separation of nano-sized ZIF-11 by centrifugation and its application in mixed matrix membranes, *J. Mater. Chem. A* 3 (2015) 6549-6556.
- [54] S.B. Wang, J.L. Lin, X.C. Wang, Semiconductor-redox catalysis promoted by metal-organic frameworks for CO<sub>2</sub> reduction, *Phys. Chem. Chem. Phys.* 16 (2014) 14656-14660.
- [55] Z. Ozturk, J.P. Hofmann, M. Lutz, M. Mazaj, N.Z. Logar, B.M. Weckhuysen, Controlled synthesis of phase-pure zeolitic imidazolate framework Co-ZIF-9, *Eur. J. Inorg. Chem.* (2015) 1625-1630.
- [56] D. Cazorla-Amoros, J. Alcaniz-Monge, M.A. de la Casa-Lillo, A. Linares-Solano, CO<sub>2</sub> as an adsorptive to characterize carbon molecular sieves and activated carbons, *Langmuir* 14 (1998) 4589-4596.
- [57] A. Berenguer-Murcia, D. Cazorla-Amoros, A. Linares-Solano, MCM-41 porosity: are surface corrugations micropores?, *Adsorpt. Sci. Technol.* 29 (2011) 443-455.
- [58] J. Liu, P.K. Thallapally, B.P. McGrail, D.R. Brown, J. Liu, Progress in adsorption-based CO<sub>2</sub> capture by metal-organic frameworks, *Chem. Soc. Rev.* 41 (2012) 2308-2322.
- [59] W.L. Qiu, L.R. Xu, C.C. Chen, D.R. Paul, W.J. Koros, Gas separation performance of 6FDA-based polyimides with different chemical structures, *Polymer* 54 (2013) 6226-6235.
- [60] M. Valero, B. Zornoza, C. Tellez, J. Coronas, Mixed matrix membranes for gas separation by combination of silica MCM-41 and MOF NH<sub>2</sub>-MIL-53(Al) in glassy polymers, *Microporous Mesoporous Mater.* 192 (2014) 23-28.
- [61] M.S. Boroglu, A.B. Yumru, Gas separation performance of 6FDA-DAM-ZIF-11 mixed-matrix membranes for H<sub>2</sub>/CH<sub>4</sub> and CO<sub>2</sub>/CH<sub>4</sub> separation, *Sep. Purif. Technol.* 173 (2017) 269-279.
- [62] B. Zornoza, B. Seoane, J.M. Zamaro, C. Tellez, J. Coronas, Combination of MOFs and zeolites for mixed-matrix membranes, *ChemPhysChem* 12 (2011) 2781-2785.
- [63] A. Galve, D. Sieffert, C. Staudt, M. Ferrando, C. Guell, C. Tellez, J. Coronas, Combination of ordered mesoporous silica MCM-41 and layered titanosilicate JDF-L1 fillers for 6FDA-based copolyimide mixed matrix membranes, *J. Membr. Sci.* 431 (2013) 163-170.

- [64] R.P. Lively, M.E. Dose, L.R. Xu, J.T. Vaughn, J.R. Johnson, J.A. Thompson, K. Zhang, M.E. Lydon, J.S. Lee, L. Liu, Z.S. Hu, O. Karvan, M.J. Realff, W.J. Koros, A high-flux polyimide hollow fiber membrane to minimize footprint and energy penalty for CO<sub>2</sub> recovery from flue gas, *J. Membr. Sci.* 423 (2012) 302-313.
- [65] B. Zornoza, C. Tellez, J. Coronas, O. Esekhiile, W.J. Koros, Mixed matrix membranes based on 6FDA polyimide with silica and zeolite microsphere dispersed phases, *AIChE J.* 61 (2015) 4481-4490.
- [66] J.H. Kim, W.J. Koros, D.R. Paul, Effects of CO<sub>2</sub> exposure and physical aging on the gas permeability of thin 6FDA-based polyimide membranes - Part 1. Without crosslinking, *J. Membr. Sci.* 282 (2006) 21-31.
- [67] M.S. Boroglu, M.A. Gurkaynak, Fabrication and characterization of silica modified polyimide-zeolite mixed matrix membranes for gas separation properties, *Polym. Bull.* 66 (2011) 463-478.
- [68] T.-S. Chung, L.Y. Jiang, Y. Li, S. Kulprathipanja, Mixed matrix membranes (MMMs) comprising organic polymers with dispersed inorganic fillers for gas separation, *Prog. Polym. Sci.* 32 (2007) 483-507.
- [69] M. Sadeghi, M.A. Semsarzadeh, H. Moadel, Enhancement of the gas separation properties of polybenzimidazole (PBI) membrane by incorporation of silica nano particles, *J. Membr. Sci.* 331 (2009) 21-30.
- [70] Y. Li, T.S. Chung, C. Cao, S. Kulprathipanja, The effects of polymer chain rigidification, zeolite pore size and pore blockage on polyethersulfone (PES)-zeolite A mixed matrix membranes, *J. Membr. Sci.* 260 (2005) 45-55.
- [71] Y. Li, H.M. Guan, T.S. Chung, S. Kulprathipanja, Effects of novel silane modification of zeolite surface on polymer chain rigidification and partial pore blockage in polyethersulfone (PES)-zeolite A mixed matrix membranes, *J. Membr. Sci.* 275 (2006) 17-28.

- [72] T.T. Moore, R. Mahajan, D.Q. Vu, W.J. Koros, Hybrid membrane materials comprising organic polymers with rigid dispersed phases, *AIChE J.* 50 (2004) 311-321.
- [73] D.Q. Vu, W.J. Koros, S.J. Miller, Mixed matrix membranes using carbon molecular sieves - II. Modeling permeation behavior, *J. Membr. Sci.* 211 (2003) 335-348.
- [74] T.T. Moore, W.J. Koros, Non-ideal effects in organic-inorganic materials for gas separation membranes, *J. Mol. Struct.* 739 (2005) 87-98.
- [75] P. Gorgojo, D. Sieffert, C. Staudt, C. Tellez, J. Coronas, Exfoliated zeolite Nu-6(2) as filler for 6FDA-based copolyimide mixed matrix membranes, *J. Membr. Sci.* 411-412 (2012) 146-152.